

tLaSDI: Thermodynamics-informed latent space dynamics identification

Jun Sur R. Park¹, Siu Wun Cheung², Youngsoo Choi²,
Yeonjong Shin^{3,4}

¹Center for Artificial Intelligence and Natural Sciences, Korea Institute for Advanced Study (KIAS), Seoul, 02455, Republic of Korea.

²Center for Applied Scientific Computing, Lawrence Livermore National Laboratory, Livermore, 94550, CA, USA.

³Department of Mathematics, North Carolina State University, Raleigh, 27695, NC, USA.

⁴Mathematical Institute for Data Science, Pohang University of Science and Technology (POSTECH), Pohang, 37673, Republic of Korea.

Contributing authors: junsurpark@kias.re.kr; cheung26@llnl.gov;
choi15@llnl.gov; yeonjong_shin@ncsu.edu;

Abstract

We propose a data-driven latent space dynamics identification method (tLaSDI) that embeds the first and second principles of thermodynamics. The latent variables are learned through an autoencoder as a nonlinear dimension reduction model. The dynamics of the latent variables are constructed by a neural network-based model that preserves certain structures to respect the thermodynamic laws through the GENERIC formalism. An abstract error estimate of the approximation is established, which provides a new loss formulation involving the Jacobian computation of autoencoder. Both the autoencoder and the latent dynamics are trained to minimize the new loss. Numerical examples are presented to demonstrate the performance of tLaSDI, which exhibits robust generalization ability, even in extrapolation. In addition, an intriguing correlation is empirically observed between the entropy production rates in the latent space and the behaviors of the full-state solution.

Keywords: reduced order model, thermodynamics, data-driven method, error estimates, dynamical systems

1 Introduction

For centuries, scientific research relied on established experiments, theories, and computational methods. First principles in physics, such as Newton’s laws, Maxwell’s equations, and the laws of thermodynamics, guided scientific exploration and fueled technological advancements in various disciplines. These principles were often derived or conceptualized by experimental or observational data. Leveraging advanced computing along with the first principles has played a pivotal role in understanding complex physical phenomena and solving challenging scientific and engineering problems. With the advent of machine learning, a data-driven scientific computing approach has drawn huge attention. The idea is to harness available data for scientific computing to complement or advance data-free approaches. Many novel methods have been proposed in this regard, e.g. [1–5].

The reduced order models (ROMs) identify intrinsic low-dimensional structures for economically representing the solution in a high-dimensional space and formulate an underlying physical process for the simplified representation. ROMs have achieved significant success in many challenging physical models such as Navier-Stokes equations [6, 7], Burgers’ equation [8–10], the Euler equations [11, 12], shallow water equations [13, 14], and Boltzmann transport problems [15]. There are two major types of ROMs in building the latent dynamics. One is intrusive and the other is non-intrusive. The projection-based ROM is a typical intrusive approach that requires invasive changes to the source code of the high-fidelity physics solver, which is not always feasible. Yet, since the projection-based approach exploits the underlying physics, it yields robust extrapolation ability. On the contrary, the non-intrusive ROM (e.g. dynamic mode decomposition [16]) does not require access to the source code, which at the same time, makes it challenging to encode underlying physical laws into the model. Thus, non-intrusive ROMs are typically regarded as black-box as it is not interpretable with existing scientific knowledge [17–19]. In building the latent space, there are two major constructions. One is the linear subspace (LS) and the other is the nonlinear manifold (NM). The LS can be efficiently constructed by the singular value decomposition on the solution snapshot matrices. However, it is limited by the assumption that the intrinsic solution space falls into a subspace with a small dimension, i.e., the solution space has a small Kolmogorov n -width. To address this limitation, the NM is proposed [20–23], which uses autoencoder for better representation ability and reconstruction accuracy.

The present work proposes a non-intrusive NM ROM method that possesses thermodynamic structures, namely, thermodynamics-informed latent space dynamics identification (tLaSDI). The general equation for the non-equilibrium reversible-irreversible coupling (GENERIC) formalism [24–26] describes a general dynamical system beyond the equilibrium, which comprises of the reversible and irreversible components. The generators for the reversible and irreversible dynamics satisfy certain conditions, which ensure the first and second principles of thermodynamics. tLaSDI uses the GENERIC formalism to design the latent dynamics and identifies the latent variables through an autoencoder [27, 28]. A distinct feature is that the latent dynamics obey the first and second laws of thermodynamics through the GENERIC

formalism and thus yield energy and entropy functions in the latent space. In particular, GENERIC formalism informed NNs (GFINNs) [29] are employed as our design choice for the latent dynamics. GFINNs are NN-based models that exactly preserve the required structures with universal approximation properties. Consequently, tLaSDI preserves the thermodynamic laws in the latent dynamics without invasive changes in the source codes. In addition, we establish an abstract error estimate of the ROM approximation (Theorem 2), which characterizes all the error components in terms of the encoder, decoder, and latent dynamics. Based on the estimate, we derive a new loss formulation on which the encoder, decoder, and thermodynamic-informed latent dynamics are simultaneously trained.

The idea of imposing thermodynamic structures in latent dynamics is not new [30–35]. Perhaps, the most relevant work to tLaSDI is [33], which proposed an NN approach to design the latent dynamics from the GENERIC formalism. However, there are several major differences. One is the choice of the models for the latent dynamics. [33] employs an NN-based model that does not satisfy the structural conditions exactly by construction, rather relies on an additional penalty term to enforce them. Another is the loss formulation. The standard loss consists of two terms - one matches the forward step prediction of the latent dynamics and the other deviates from the autoencoder. The proposed new loss function introduces additional two loss terms that involve Jacobian, which turns out to bring significant improvements in generalization ability. The last one is the way the latent variables and dynamics are trained. [33] learns the latent variables separately, independent of latent dynamics. The latent dynamics are then trained later to fit the fixed latent variables. This separate training approach has been adopted in the literature, e.g., see [17, 34]. In contrast, tLaSDI uses the simultaneous training approach that trains the latent variables and their dynamics at the same time. This strategy has been employed in the literature as well, e.g., see [18, 19, 32, 36, 37].

Several numerical experiments are reported to demonstrate the performance of tLaSDI and verify the effectiveness of the new loss function. Results show that tLaSDI exhibits robust extrapolation ability, which pure data-driven approaches typically lack. Also, it is empirically observed that the latent entropy function manifests a correlated behavior aligned with the full-state solution. For the parametric Burgers’ equation, the rate of entropy production has the largest value at the final time when the solution exhibits the stiffest behavior. In contrast, the entropy production rate for the heat equation behaves the opposite as it saturates as time goes on, which aligns with the solution behavior of the heat equation. See Figures 7 and 8.

The rest of the paper is organized as follows. Section 2 describes the problem setup and some preliminaries. The proposed method, tLaSDI, is presented in Section 3 along with the new loss formulation. Section 4 is devoted to the abstract error estimate. Numerical examples are presented in Section 5 before the conclusions in Section 6.

2 Preliminaries and problem formulation

Let us consider a dynamical system (the full-order model)

$$\dot{\mathbf{x}}_\mu(t) = F_\mu(\mathbf{x}_\mu(t), t) \quad \forall t > 0 \quad \text{with } \mathbf{x}_\mu(0) = \mathbf{x}^0(\mu) \in \mathbb{R}^N, \quad (2.1)$$

defined in a high dimensional space \mathbb{R}^N , where μ represents some parameters of interest in Ω_μ and F_μ is an appropriate field function that guarantees the existence of the solution to (2.1) for all $\mu \in \Omega_\mu$.

Since the state dimension is very large, i.e., $N \gg 1$, a direct numerical simulation is computationally costly, prohibiting multiple simulations at varying μ . Even worse, numerical simulations are not possible if F_μ is unknown. The non-intrusive ROM can be used in this regard to achieve the following two goals.

- **Computational savings:** When F_μ is fully known, the goal of ROM is to reduce the computational time in simulating the full-order dynamics at multiple μ . It requires the full-state solution data at selected parameters from direct numerical simulations of (2.1). The quality of the ROM approximation is measured by the prediction accuracy on unseen parameters. In particular, it is popularly used for parametric partial differential equations (PDE) problems.
- **Data-driven discovery of dynamical systems:** When F_μ is not available, the goal of ROM is to learn a dynamical system from data that produces trajectories that are similar to data (interpolation) or predict states in future times (extrapolation). Here the trajectory data is assumed to be given. The pure data-driven approach, however, is known to lack robust extrapolation ability. This is the task where the intrusive ROM is not applicable as F_μ is unknown.

In the ROM framework, the full-state variables $\mathbf{x} \in \mathbb{R}^N$ are transformed to the so-called latent variables $\mathbf{z} \in \mathbb{R}^n$ that lie in a much lower dimensional space, i.e., $n \ll N$. Such a mapping is called an encoder $\phi_e(\cdot) : \mathbb{R}^N \rightarrow \mathbb{R}^n$. Given an encoder, a latent dynamical system is formed

$$\dot{\mathbf{z}}_\mu(t) = F_\mu^r(\mathbf{z}_\mu(t), t) \quad \forall t > 0 \quad \text{with } \mathbf{z}_\mu(0) = \phi_e(\mathbf{x}_\mu(0)) \in \mathbb{R}^n. \quad (2.2)$$

Lastly, a decoder function $\phi_d(\cdot) : \mathbb{R}^n \rightarrow \mathbb{R}^N$ transforms the latent variables back to the original full-order space, providing the ROM approximation to $\mathbf{x}_\mu(t)$:

$$\tilde{\mathbf{x}}_\mu(t) = \phi_d(\mathbf{z}_\mu(t)),$$

where \mathbf{z}_μ is the solution to (2.2).

The constructions of the encoder, decoder, and latent dynamics determine a specific ROM method. In general, such constructions are obtained from data. Here the data refers to a set of either direct numerical simulations of (2.1) or a collection of spatiotemporal trajectories. The present work focuses on developing a new NN-based model for latent dynamics to be learned from data while leveraging nonlinear dimension reduction via autoencoder.

2.1 Neural networks

A L -layer feed-forward NN is a function $f_{\text{NN}} : \mathbb{R}^{d_{\text{in}}} \ni x \mapsto f^L(x) \in \mathbb{R}^{d_{\text{out}}}$ defined recursively according to

$$f^l(x) = W^l \sigma(f^{l-1}(x)) + b^l, \quad 2 \leq l \leq L,$$

with $f^1(x) = W^1 x + b^1$. The activation function σ is a scalar function defined on \mathbb{R} applied in element-wise. It is typically chosen to satisfy the conditions of the universal approximation theorem [38–40]. $W^l \in \mathbb{R}^{n_l \times n_{l-1}}$ and $b^l \in \mathbb{R}^{n_l}$ are the weight matrix and the bias vector of the l -th layer, respectively, where $n_0 = d_{\text{in}}$, $n_L = d_{\text{out}}$. The collection of all the weight matrices and bias vectors is denoted by $\boldsymbol{\theta}$. To explicitly acknowledge the dependency of $\boldsymbol{\theta}$, the NN is often denoted as $f_{\text{NN}}(\cdot; \boldsymbol{\theta})$.

In the parametric dynamical systems, it is often needed to let the NN parameters depend on $\mu \in \Omega_p$ to enhance the flexibility and prediction accuracy. The hypernetwork [41] is a NN model designed for this purpose, which introduces another NN that takes μ as input and outputs the network parameter $\boldsymbol{\theta}(\mu)$ of f_{NN} . Accordingly, the hypernetwork is denoted by $f_{\text{NN}}(\cdot; \boldsymbol{\theta}(\mu))$.

The autoencoder (AE) is an NN-based model designed for dimension reduction, which comprises of an encoder $\phi_e(\cdot; \boldsymbol{\theta}_e) : \mathbb{R}^N \rightarrow \mathbb{R}^n$ and a decoder $\phi_d(\cdot; \boldsymbol{\theta}_d) : \mathbb{R}^n \rightarrow \mathbb{R}^N$ where $\boldsymbol{\theta}_e$ and $\boldsymbol{\theta}_d$ are the NN parameters for the encoder and decoder respectively. The autoencoder takes high-dimensional inputs \boldsymbol{x} and transforms it to the so-called latent variables \boldsymbol{z} through the encoder. The decoder then takes \boldsymbol{z} and returns high-dimensional variables $\hat{\boldsymbol{x}}$ having the same size as the original inputs. Ideally, the autoencoder is trained to reconstruct the original inputs, i.e., $\boldsymbol{x} \approx \hat{\boldsymbol{x}} = \phi_d(\phi_e(\boldsymbol{x}; \boldsymbol{\theta}_e); \boldsymbol{\theta}_d)$.

2.2 GENERIC formalism

The GENERIC formalism [24, 26] is a mathematical framework that encompasses both conservative and dissipative systems, providing a comprehensive description of beyond-equilibrium thermodynamic systems. The formalism describes the dynamical systems involving four functions – the scalar functions E and S that represent the total energy and entropy of the system respectively, and the matrix-valued functions L and M called the Poisson and the friction matrices, respectively;

$$\begin{aligned} \dot{\boldsymbol{z}} &= L(\boldsymbol{z}) \nabla E(\boldsymbol{z}) + M(\boldsymbol{z}) \nabla S(\boldsymbol{z}), \\ \text{subject to } L(\boldsymbol{z}) \nabla S(\boldsymbol{z}) &= M(\boldsymbol{z}) \nabla E(\boldsymbol{z}) = \mathbf{0}, \\ L(\boldsymbol{z}) &\text{ is skew-symmetric, i.e., } L(\boldsymbol{z}) = -L(\boldsymbol{z})^\top, \\ M(\boldsymbol{z}) &\text{ is symmetric \& positive semi-definite.} \end{aligned} \tag{2.3}$$

The degeneracy conditions guarantee the first and second laws of thermodynamics, i.e., the following properties of energy conservation and non-decreasing entropy, as $\frac{d}{dt} E(\boldsymbol{z}) = 0$ and $\frac{d}{dt} S(\boldsymbol{z}) \geq 0$.

GFINNs: Several NN-based models were proposed to embed the GENERIC formalism [29, 42, 43]. In particular, we briefly review the model proposed in [29], namely,

GFINNs. We direct readers to refer to [29] for more details. The GFINNs comprise of four NNs – E_{NN} , S_{NN} , L_{NN} and M_{NN} – that represent NN approximations to E , S , L and M in (2.3), respectively. These NNs are designed to exactly satisfy the degeneracy conditions in (2.3) while also being adequately expressive to capture the underlying dynamics from data. The GFINN construction is based on the following theorem [29].

Theorem 1 (Lemma 3.6 of [29]). *Let A_j be a skew-symmetric matrix of size $n \times n$, $j = 1, \dots, m$ and $g(\cdot) : \mathbb{R}^n \rightarrow \mathbb{R}$ a differentiable scalar function. For the matrix valued function $Q_g(\cdot) : \mathbb{R}^n \rightarrow \mathbb{R}^{m \times n}$ whose j -th row is defined as $(A_j \nabla g(\cdot))^\top$, we have $Q_g(\mathbf{z}) \nabla g(\mathbf{z}) = \mathbf{0}$ for all $\mathbf{z} \in \mathbb{R}^n$.*

Let S_{NN} be a feed-forward NN and consider the associated matrix-valued function $Q_{S_{\text{NN}}}$ according to Theorem 1. The NN model L_{NN} for the Poisson matrix is then constructed by

$$L_{\text{NN}}(\mathbf{z}) := (Q_{S_{\text{NN}}}(\mathbf{z}))^\top U_{\text{NN}}(\mathbf{z}) Q_{S_{\text{NN}}}(\mathbf{z}),$$

where $U_{\text{NN}}(\mathbf{z}) : \mathbb{R}^n \rightarrow \mathbb{R}^{m \times n}$ is a skew symmetric matrix-valued NN. It can be readily checked that the degeneracy condition and the symmetry of the matrix functions are exactly satisfied by the above construction. M_{NN} and E_{NN} are similarly built. Furthermore, such construction enjoys a universal approximation property as shown in [29].

3 Thermodynamics-informed learning for latent space dynamics

We propose the thermodynamics-informed latent dynamics identification (tLaSDI) method, which designs the latent space dynamics as an NN-based model that embeds the first and second laws of thermodynamics through the GENERIC formalism.

In particular, we propose to design the latent dynamics F_μ^r in the ROM (2.2) from the GENERIC formalism. While some alternatives [33, 43] are equally applicable, we confine ourselves to GFINNs [29] for the sake of simplicity of discussion. For latent manifold learning, we propose the hyper-autoencoder that combines the hypernetworks [41, 44] and the autoencoder to further improve the performance in the parametric cases. That is, the hyper-encoder $\phi_e(\cdot; \boldsymbol{\theta}_e(\mu))$ and the hyper-decoder $\phi_d(\cdot; \boldsymbol{\theta}_d(\mu))$ are employed. The schematic description of the model for tLaSDI is illustrated in Figure 1.

Remark 1. [42] is the first work that proposed an NN-based model to encode the GENERIC formalism, namely, Structure-Preserving NN (SPNN). While SPNN aims to enforce the degeneracy conditions through an additional loss term that penalizes these conditions, in principle, it does not satisfy them exactly. [43] proposed a model, namely, GNODE, which satisfies the degeneracy conditions exactly without any additional loss term, however, does not have universal approximation properties. The NN model of [29], namely, GFINNs is the one that comes with the exact degeneracy conditions and the universal approximation properties.

3.1 tLaSDI: Loss formulation

We present a novel loss formulation for tLaSDI, which is derived from an abstract error estimate presented in Section 4.

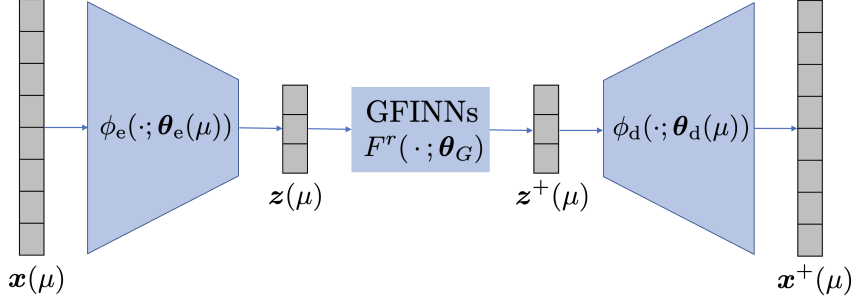


Fig. 1: The schematic NN model of tLaSDI. The hyper-autoencoder is used for the parametric dynamical systems. The latent dynamics are modelled by GFINNs.

For a given parameter $\mu \in \Gamma_{\text{train}}$, let $\{\mathbf{x}_\mu^k := \mathbf{x}_\mu(t_k)\}_{k \geq 0}$ be a collection of full-state trajectory data/snapshots. Assuming the time step is sufficiently small, one may also obtain the (approximated) derivatives $\{\dot{\mathbf{x}}_\mu^k\}_{k \geq 0}$. For example, the central difference formula gives $\dot{\mathbf{x}}_\mu^k \approx (\mathbf{x}_\mu^{k+1} - \mathbf{x}_\mu^{k-1})/2\Delta t$. While the approximation errors exist, for simplicity of notation, we denote the approximated derivatives by $\dot{\mathbf{x}}_\mu^k$ with slight abuse of notation.

We then propose to train the tLaSDI to minimize the loss function defined by

$$\mathcal{L}(\boldsymbol{\theta}) = \lambda_{\text{int}} \mathcal{L}_{\text{int}}(\boldsymbol{\theta}) + \lambda_{\text{rec}} \mathcal{L}_{\text{rec}}(\boldsymbol{\theta}) + \lambda_{\text{Jac}} \mathcal{L}_{\text{Jac}}(\boldsymbol{\theta}) + \lambda_{\text{mod}} \mathcal{L}_{\text{mod}}(\boldsymbol{\theta}), \quad (3.1)$$

where $\boldsymbol{\theta} = \{\boldsymbol{\theta}_e, \boldsymbol{\theta}_d, \boldsymbol{\theta}_G\}$ is the collection of all the trainable parameters. The loss function consists of four components – $\mathcal{L}_{\text{int}}, \mathcal{L}_{\text{rec}}, \mathcal{L}_{\text{Jac}}, \mathcal{L}_{\text{mod}}$ – the subscripts stand for ‘integration’, ‘reconstruction’, ‘Jacobian’ and ‘model’, respectively. The first two terms $\mathcal{L}_{\text{int}}, \mathcal{L}_{\text{rec}}$ are commonly employed in the context of the data-driven discovery of dynamical systems [33, 34, 37] and the last term \mathcal{L}_{mod} was introduced in [18, 36, 45]. The Jacobian loss term \mathcal{L}_{Jac} is newly proposed in the present work. The error estimate in Section 4 provides a theoretical justification for the use of the loss function (3.1).

Remark 2. *The latter two loss terms utilize the derivative information. When the derivative of data is not available, while the fourth term shall be dropped, the third term can be revised to avoid using the derivatives. See the details below.*

The integration loss is a commonly employed term for learning problems in dynamical systems. It measures the discrepancy between the latent state from the encoder at \mathbf{x}_μ^{k+1} and the corresponding one-time step integration of the latent dynamics starting at the latent state from the encoder at the previous time \mathbf{x}_μ^k . That is, the term enforces

$$\phi_e(\mathbf{x}_\mu^{k+1}) \approx \phi_e(\mathbf{x}_\mu^k) + \int_{t_k}^{t_{k+1}} F_\mu^r(\mathbf{z}_\mu(t), t) dt.$$

By summing it over all the data, the integral loss is defined by

$$\mathcal{L}_{\text{int}} = \sum_{\mu \in \Gamma_{\text{train}}} \sum_k \left\| \phi_e(\mathbf{x}_\mu^{k+1}) - \phi_e(\mathbf{x}_\mu^k) - \int_{t_k}^{t_{k+1}} F_\mu^r(\mathbf{z}_\mu(t), t) dt \right\|_2^2,$$

where t_k represents the time after k -th time steps and the integral is approximated by employing a numerical integrator (e.g., Runge-Kutta methods). It is worth noting that the integration loss is independent of the decoder.

The reconstruction loss is another standard loss term when it comes to training autoencoder. It measures the discrepancy between the full-state data and the autoencoder reconstruction. The term particularly takes into account the autoencoder's ability to reconstruct the high-dimensional original data and is defined by

$$\mathcal{L}_{\text{rec}} = \sum_{\mu \in \Gamma_{\text{train}}} \sum_k \|\mathbf{x}_\mu^k - \phi_d \circ \phi_e(\mathbf{x}_\mu^k)\|_2^2.$$

The Jacobian loss is the term derived from the abstract error estimates of the ROM approximation (Section 4). The term requires the (approximated) derivative data of the full-state dynamics and measures the time derivative of the reconstruction error, i.e.,

$$\frac{d}{dt} (\mathbf{x}_\mu^k - \phi_d \circ \phi_e(\mathbf{x}_\mu^k)) = (I - J(\mathbf{x}_\mu^k)) \dot{\mathbf{x}}_\mu^k,$$

where $J(\mathbf{x}_\mu^k) := J_d(\phi_e(\mathbf{x}_\mu^k))J_e(\mathbf{x}_\mu^k)$ is the Jacobian of the autoencoder and I is the identity matrix. The Jacobian loss is then given by

$$\mathcal{L}_{\text{Jac}} = \sum_{\mu \in \Gamma_{\text{train}}} \sum_k \|(I - J(\mathbf{x}_\mu^k)) \dot{\mathbf{x}}_\mu^k\|_2^2. \quad (3.2)$$

While the loss term may be viewed as a heuristic Sobolev-type loss for the reconstruction loss (which introduces a high-order derivative in the loss), our motivation for introducing the Jacobian loss stems from Theorem 2 as an effort to minimize an upper bound of the error.

In the case where accurate derivative data are not available, one may revise the Jacobian loss by observing

$$\|(I - J(\mathbf{x}_\mu^k)) \dot{\mathbf{x}}_\mu^k\|_2 \leq \|I - J(\mathbf{x}_\mu^k)\|_2 \cdot \|\dot{\mathbf{x}}_\mu^k\|_2 \leq \|I - J(\mathbf{x}_\mu^k)\|_F \cdot \|\dot{\mathbf{x}}_\mu^k\|_2,$$

where $\|\cdot\|_F$ is the Frobenius norm. The revised Jacobian loss may be given by

$$\mathcal{L}_{\text{Jac}} = \sum_{\mu \in \Gamma_{\text{train}}} \sum_k \|I - J(\mathbf{x}_\mu^k)\|_F^2,$$

which does not require the derivative information.

The model loss may be viewed as a complement term to the Jacobian loss. Since the dimension of the latent variables is smaller than the full-state dimension, the Jacobian of the autoencoder can never be a full rank, which implies $J(\cdot) \neq I$. Therefore, one may design another loss from the following observation.

$$\begin{aligned} \|(I - J(\mathbf{x}_\mu^k)) \dot{\mathbf{x}}_\mu^k\|_2 &\leq \|\dot{\mathbf{x}}_\mu^k - J_d(\phi_e(\mathbf{x}_\mu^k)) F_\mu^r \circ \phi_e(\mathbf{x}_\mu^k)\|_2 \\ &\quad + \|J_d(\phi_e(\mathbf{x}_\mu^k))\| \cdot \|J_e(\mathbf{x}_\mu^k) \dot{\mathbf{x}}_\mu^k - F_\mu^r \circ \phi_e(\mathbf{x}_\mu^k)\|_2. \end{aligned}$$

The first term on the right-hand side measures the modeling error of the full-order dynamics. Ideally, since $\dot{\mathbf{x}}_\mu^k = F(\mathbf{x}_\mu^k)$, the corresponding NN construction via the latent space dynamics is $J_d(\phi_e(\mathbf{x}_\mu^k)) F_\mu^r \circ \phi_e(\mathbf{x}_\mu^k)$. This means that the first term measures how well the NN construction approximates the underlying full-order dynamics through the derivative data.

The second term on the right-hand side involves with $\|J_e(\mathbf{x}_\mu^k) \dot{\mathbf{x}}_\mu^k - F_\mu^r \circ \phi_e(\mathbf{x}_\mu^k)\|_2$, which can be interpreted as the modeling error of the latent dynamics. If the encoder were given, $J_e(\mathbf{x}_\mu^k) \dot{\mathbf{x}}_\mu^k$ describes the underlying latent space dynamics derived from the full-order dynamics $\dot{\mathbf{x}}_\mu^k = F(\mathbf{x}_\mu^k)$. Since $F_\mu^r \circ \phi_e(\mathbf{x}_\mu^k)$ represents our model for the latent dynamics, the discrepancy between the two terms measures the approximation (or modeling) error of the latent space dynamics via F_μ^r . Altogether leads to the model loss defined by

$$\mathcal{L}_{\text{mod}} = \sum_{\mu \in \Gamma_{\text{train}}} \sum_k \|J_e(\mathbf{x}_\mu^k) \dot{\mathbf{x}}_\mu^k - F_\mu^r \circ \phi_e(\mathbf{x}_\mu^k)\|_2^2 + \|\dot{\mathbf{x}}_\mu^k - J_d(\phi_e(\mathbf{x}_\mu^k)) F_\mu^r \circ \phi_e(\mathbf{x}_\mu^k)\|_2^2.$$

Lastly, we note that, unlike the Jacobian loss, the model loss requires one to have the derivative information.

The Jacobian and model loss terms require the computation of Jacobian matrices, which can be efficiently evaluated by leveraging the Jacobian-vector product (JVP) feature provided by PyTorch [46] or JAX [47]. A simple Pytorch snippet for JVP is presented to illustrate its simplicity:

```
J_e = torch.autograd.functional.jvp(encoder, x, dx) [1]
J_d = torch.autograd.functional.jvp(decoder, z, dz) [1]
```

The presented framework trains the encoder, decoder, and latent dynamics simultaneously to minimize the loss function (3.1). This simultaneous training has been used in the literature [18, 19, 32, 36, 37]. Since tLaSDI imposes a thermodynamic structure on the latent state dynamics, this comes as a natural choice because the latent variables found by the autoencoder shall be compatible with the imposed structure (thermodynamics). We, however, acknowledge other works (e.g. [17, 33, 34]) that train the autoencoder separately as a data preprocessing and then learn the latent dynamics from the fixed latent states. Empirically, we found that tLaSDI performs significantly better when it is trained simultaneously. This may indicate that the imposed underlying structure on the latent dynamics may play a key role in this regard, which facilitates the interaction between the autoencoder and the NN-based latent dynamics.

4 Abstract error estimate

We present an abstract error estimate, which reveals all the components attributing the total errors of the ROM approximation. For ease of discussion, without loss of generality, we suppress all the parametric dependencies.

Let $\mathbf{x}(t)$ be the solution to the full-order model of $\dot{\mathbf{x}} = F(\mathbf{x})$. We are interested in estimating the ROM approximation error, i.e.,

$$e(t; t_0) := \mathbf{x}(t) - \phi_d \left(\phi_e(\mathbf{x}(t_0)) + \int_{t_0}^t F^r(\mathbf{z}(s)) ds \right),$$

where \mathbf{z} is the solution of the latent space dynamics (2.2) satisfying $\mathbf{z}(t_0) = \phi_e(\mathbf{x}(t_0))$.

Theorem 2. *Let \mathbf{x} be the solution to the full-order model $\dot{\mathbf{x}} = F(\mathbf{x})$, and let \mathbf{z} be the solution to the latent dynamics of $\dot{\mathbf{z}} = F^r(\mathbf{z})$ with $\mathbf{z}(t_0) = \phi_e(\mathbf{x}(t_0))$. Suppose the Jacobian of the decoder ϕ_d is Lipschitz continuous and bounded, and F^r is bounded. For any $t > t_0$, the ROM error is bounded by*

$$\|e(t; t_0)\| \lesssim \varepsilon_{\text{int}}(t; t_0) + \varepsilon_{\text{rec}}(t; t_0) + \varepsilon_{\text{Jac}}(t; t_0) + \varepsilon_{\text{mod}}(t; t_0),$$

where each error term is defined by

$$\begin{aligned} \varepsilon_{\text{int}}(t; t_0) &= \int_{t_0}^t \|\phi_e(\mathbf{x}) - \mathbf{z}\| ds, \\ \varepsilon_{\text{rec}}(t; t_0) &= \|\mathbf{x}(t_0) - (\phi_d \circ \phi_e)(\mathbf{x}(t_0))\| + \|\mathbf{x}(t) - (\phi_d \circ \phi_e)(\mathbf{x}(t))\|, \\ \varepsilon_{\text{Jac}}(t; t_0) &= \int_{t_0}^t \|(I - J(\mathbf{x}(s)))\dot{\mathbf{x}}(s)\| ds, \\ \varepsilon_{\text{mod}}(t; t_0) &= \int_{t_0}^t \left(\|J_e(\mathbf{x})\dot{\mathbf{x}} - F^r(\mathbf{z})\| + \|\dot{\mathbf{x}} - J_d(\mathbf{z})F^r(\mathbf{z})\| \right) ds, \end{aligned}$$

and \lesssim hides unimportant constants.

Proof. Let $\hat{\mathbf{x}}(t) = (\phi_d \circ \phi_e)(\mathbf{x}(t))$, which can be interpreted as the reconstructed full-state dynamics from the autoencoder. Since $\dot{\mathbf{x}}(t) = F(\mathbf{x}(t))$, it follows from the chain rule that the dynamics of $\hat{\mathbf{x}}$ is described by

$$\dot{\hat{\mathbf{x}}} = J_d(\phi_e(\mathbf{x})) J_e(\mathbf{x}) F(\mathbf{x}) \quad \forall t > 0, \quad \hat{\mathbf{x}}(t_0) = (\phi_d \circ \phi_e)(\mathbf{x}(t_0)).$$

Since the dynamics of $\hat{\mathbf{x}}$ require the original full-state dynamics F , it is not available in practice. Yet, this serves as an idealized model to be learned for the ROM. Let $e_{\text{ideal}}(t) := \mathbf{x}(t) - \hat{\mathbf{x}}(t)$. It then can be checked that the ideal error e_{ideal} is governed by

$$\dot{e}_{\text{ideal}} = (I - J(\mathbf{x}))F(\mathbf{x}) \quad \forall t, \quad e_{\text{ideal}}(t_0) = \mathbf{x}(t_0) - (\phi_d \circ \phi_e)(\mathbf{x}(t_0)).$$

By integrating over time, we obtain $e_{\text{ideal}}(t) = e_{\text{ideal}}(t_0) + \int_{t_0}^t (I - J(\mathbf{x}(s)))F(\mathbf{x}(s))ds$, which gives

$$\|e_{\text{ideal}}(t)\| \leq \alpha \left(\|e_{\text{ideal}}(t_0)\| + \int_{t_0}^t \|(I - J(\mathbf{x}(s)))\dot{\mathbf{x}}(s)\| ds \right) + (1 - \alpha)\|e_{\text{ideal}}(t)\|,$$

for any $\alpha \in (0, 1)$.

Let $\tilde{\mathbf{x}}(t) = \phi_d \left(\phi_e(\mathbf{x}(t_0)) + \int_{t_0}^t F^r(\mathbf{z}(s))ds \right)$ where \mathbf{z} is the solution to $\dot{\mathbf{z}} = F^r(\mathbf{z})$ with $\mathbf{z}(t_0) = \phi_e(\mathbf{x}(t_0))$. We note that $\tilde{\mathbf{x}}$ is the one constructed from the ROM framework that uses both the autoencoder and the latent dynamics. Let $e_{\text{ROM}}(t) = \tilde{\mathbf{x}}(t) - \hat{\mathbf{x}}(t)$ be the error between the ROM reconstruction and the ideal reconstruction. It then can be checked that the error is governed by

$$\dot{e}_{\text{ROM}} = J(\mathbf{x})F(\mathbf{x}) - J_d(\mathbf{z})F^r(\mathbf{z}) \quad \forall t, \quad e_{\text{ROM}}(t_0) = 0.$$

For any $\alpha \in (0, 1)$, since

$$\begin{aligned} \|J(\mathbf{x})F(\mathbf{x}) - J_d(\mathbf{z})F^r(\mathbf{z})\| &\leq \alpha \|J_d(\phi_e(\mathbf{x}))\| \cdot \|J_e(\mathbf{x})F(\mathbf{x}) - F^r(\mathbf{z})\| \\ &\quad + \alpha \|J_d(\phi_e(\mathbf{x})) - J_d(\mathbf{z})\| \cdot \|F^r(\mathbf{z})\| \\ &\quad + (1 - \alpha)\|(I - J(\mathbf{x}))F(\mathbf{x})\| \\ &\quad + (1 - \alpha)\|F(\mathbf{x}) - J_d(\mathbf{z})F^r(\mathbf{z})\|, \end{aligned}$$

it follows from the Lipschitz continuities of ϕ_d , J_d and the boundedness of F^r that

$$\begin{aligned} \|e_{\text{ROM}}(t)\| &\lesssim \int_{t_0}^t \|J_e(\mathbf{x})F(\mathbf{x}) - F^r(\mathbf{z})\| ds + \int_{t_0}^t \|\phi_e(\mathbf{x}) - \mathbf{z}\| ds \\ &\quad + \int_{t_0}^t \|(I - J(\mathbf{x}))F(\mathbf{x})\| + \|F(\mathbf{x}) - J_d(\mathbf{z})F^r(\mathbf{z})\| ds. \end{aligned}$$

Therefore, by combining the above estimates, we obtain

$$\begin{aligned} \|\mathbf{x}(t) - \tilde{\mathbf{x}}(t)\| &\lesssim \int_{t_0}^t \|\phi_e(\mathbf{x}) - \mathbf{z}\| ds + \|e_{\text{ideal}}(0)\| + \|e_{\text{ideal}}(t)\| \\ &\quad + \int_{t_0}^t \|(I - J(\mathbf{x}(s)))\dot{\mathbf{x}}(s)\| ds \\ &\quad + \int_{t_0}^t \left(\|J_e(\mathbf{x})F(\mathbf{x}) - F^r(\mathbf{z})\| + \|F(\mathbf{x}) - J_d(\mathbf{z})F^r(\mathbf{z})\| \right) ds, \end{aligned}$$

which completes the proof. \square

For a small time interval $[t_k, t_{k+1}]$, if \mathbf{z} satisfies $\mathbf{z}(t_k) = \phi_e(\mathbf{x}(t_k))$, we have

$$\varepsilon_{\text{int}}(t_{k+1}; t_k) = \int_{t_k}^{t_{k+1}} \|\phi_e(\mathbf{x}) - \mathbf{z}\| ds \approx \frac{\Delta t}{2} \cdot \|\phi_e(\mathbf{x}(t_{k+1})) - \mathbf{z}(t_{k+1})\|,$$

where the integral is approximated by the trapezoidal rule. Since $\dot{\mathbf{z}} = F^r(\mathbf{z})$, it can be checked that

$$\varepsilon_{\text{int}}(t_{k+1}; t_k) \approx \frac{\Delta t}{2} \cdot \left\| \phi_e(\mathbf{x}(t_{k+1})) - \phi_e(\mathbf{x}(t_k)) - \int_{t_k}^{t_{k+1}} F^r(\mathbf{z}(s)) ds \right\|,$$

and from which, one can discover the integration loss \mathcal{L}_{int} . By following a similar argument, all the loss terms of (3.1) can be discovered from the corresponding error components of Theorem 2.

Since the result of Theorem 2 is general and abstract, it could be used for estimating the error of any ROM approximation. For example, suppose $F(\mathbf{x}) = M\mathbf{x}$ is linear where $M = [Q, \tilde{Q}] \begin{bmatrix} \Sigma \\ \tilde{\Sigma} \end{bmatrix} \begin{bmatrix} Q^\top \\ \tilde{Q}^\top \end{bmatrix}$ is a spectral decomposition, and the encoder and decoder are also linear, say, $\phi_e(\mathbf{x}) = Q^\top \mathbf{x}$ and $\phi_d(\mathbf{z}) = Q\mathbf{z}$ with $Q^\top Q = I$. Since the projection-based LS-ROM uses $F^r(\mathbf{z}) = Q^\top M Q \mathbf{z} = \Sigma \mathbf{z}$ as the latent dynamics, it can be checked that

$$\begin{aligned} \phi_e(\mathbf{x}) - \mathbf{z} &= Q^\top \mathbf{x} - \mathbf{z}, \\ (I - J(\mathbf{x}))\dot{\mathbf{x}} &= (I - Q Q^\top) M \mathbf{x} = \tilde{Q} \tilde{\Sigma} \tilde{Q}^\top \mathbf{x}, \\ F(\mathbf{x}) - J_d(\mathbf{z}) F^r(\mathbf{z}) &= Q \Sigma (Q^\top \mathbf{x} - \mathbf{z}) + \tilde{Q} \tilde{\Sigma} \tilde{Q}^\top \mathbf{x}, \\ J_e(\mathbf{x}) F(\mathbf{x}) - F^r(\mathbf{z}) &= \Sigma (Q^\top \mathbf{x} - \mathbf{z}). \end{aligned}$$

Since $Q^\top \mathbf{x} = \mathbf{z}$ as it matches the initial condition, the error estimate of Theorem 2 yields

$$\|e(t; t_0)\| \lesssim \|\tilde{Q} \tilde{Q}^\top \mathbf{x}(t_0)\| + \int_{t_0}^t \|\tilde{Q} \tilde{\Sigma} \tilde{Q}^\top \mathbf{x}\| ds.$$

The error estimate provides a theoretical foundation for the proposed loss function (3.1) and explains the role of each loss component. Some loss terms were introduced in [18, 36] in a heuristic way, while Theorem 2 provides a solid theoretical justification for them. The advantage of the new loss will be demonstrated through numerical experiments in Section 5.

5 Numerical examples

This section presents numerical examples to demonstrate the effectiveness of tLaSDI. Two learning tasks are considered. One is the data-driven discovery of dynamical systems to predict the trajectories in future times (extrapolation). The other task focuses on the parametric PDE problems.

All the implementations were done on a Livermore Computing Lassen system's NVIDIA V100 (Volta) GPU, located at the Lawrence Livermore National Laboratory. This GPU is equipped with 3,168 NVIDIA CUDA Cores and possesses 64 GB of GDDR5 GPU Memory. The source codes are written in the open-source PyTorch [46] and will be published in GitHub.

5.1 Data-driven discovery of dynamical systems: Extrapolation

For the data-driven discovery of dynamics, we consider the non-parametric full-order dynamics, which corresponds to $|\Omega_\mu| = 1$. The extrapolation predicts the full-state solution at times outside of the training range. For numerical experiments, we divide the given trajectory data of the time range $[0, T + \delta]$ into two. One contains the trajectory of $[0, T]$, which is used for training. The other contains the remaining one of $(T, T + \delta]$, which is used for testing. The extrapolation accuracy is measured by the averaged relative ℓ_2 error over time:

$$e_{\mathbf{x}}^{\ell_2} = \frac{1}{|\kappa_{\text{test}}|} \sum_{k \in \kappa_{\text{test}}} \left(\frac{\|\mathbf{x}^k - \tilde{\mathbf{x}}^k\|_2}{\|\mathbf{x}^k\|_2} \right), \quad (5.1)$$

where $\kappa_{\text{test}} = \{k \mid t_k \in (T, T + \delta]\}$ and $\tilde{\mathbf{x}}^k$ is the ROM prediction at time t_k computed with the initial condition of $x_\mu(T)$. (5.1) is referred to as the extrapolation error.

tLaSDI is compared with two NM ROM methods. One is the Vanilla-FNN, which uses plain feed-forward NNs for the encoder, decoder, and latent dynamics and trains them on the standard loss function which contains the first two loss terms of (3.1). TA-ROM [33] uses the sparse autoencoder and then models the latent dynamics using SPNN [33, 42]. This method follows the separate training schemes and uses the standard loss function. Other details of Vanilla-FNN and TA-ROM can be found in Appendix A.

NN architectures are chosen to be comparable with each other in terms of the number of NN parameters. Adam [48] optimizer is employed throughout for the training.

5.1.1 Couette flow of an Oldroyd-B fluid

The Couette flow of an Oldroyd-B fluid model describes viscoelastic fluids composed of linear elastic dumbbells representing polymer chains in a solvent. The model involves four state variables for all 100 nodes. The state variables for the i -th node are the fluid’s position on each mesh node (q_i), its velocity in the x -direction (v_i), internal energy (e_i), and the shear component (τ_i) of the conformation tensor.

Following [33, 42], we construct the full-order state by concatenating all the variables, i.e., $\mathbf{x}(t) = [\mathbf{q}(t) \ \mathbf{v}(t) \ \mathbf{e}(t) \ \boldsymbol{\tau}(t)]^\top \in \mathbb{R}^{400}$, where $\mathbf{q} = [q_1 \dots q_{100}]$, $\mathbf{v} = [v_1 \dots v_{100}]$, $\mathbf{e} = [e_1 \dots e_{100}]$, and $\boldsymbol{\tau} = [\tau_1 \dots \tau_{100}]$. Consequently, the dimension of the full-order model is 400. We set $T = 0.9$, $\delta = 0.1$ with the fixed time step of $\Delta t = \frac{1}{150}$.

In all the methods, the autoencoders contain 183K trainable parameters with the latent space dimension of $n = 8$. For the latent space dynamics, Vanilla-FNN, TA-ROM, and tLaSDI consist of 143K, 125K, and 139K parameters, respectively. All methods were trained for approximately 2500 seconds of wall-clock time resulting in around 20K and 140K iterations for tLaSDI and Vanilla-FNN respectively. For TA-ROM, SAE and SPNN undergo training for 26K and 180K iterations respectively, leading to a total of 206K iterations. The number of iterations for SAE and SPNN in TA-ROM is carefully selected regarding the extrapolation performance. Other implementation details can be found in Appendix B.1.

Figure 2 shows the training loss and extrapolation error trajectories by the three different methods with respect to the wall-clock time in seconds. We run 10 independent simulations and report all the training trajectories on the left. It can be seen that the training losses are separated by each method. This is expected as each method has its own training loss and they scale differently. Regardless, we see that all the losses saturate at the end of the training. Since TA-ROM sequentially trains SAE and SPNN in that order, the part before the black vertical dashed line corresponds to the SAE training and the rest falls into the SPNN training. It is seen in the latent dynamics training for TA-ROM that the training loss trajectories are significantly different by several orders of magnitude, which causes a large variance in extrapolation errors. On the right, we report the extrapolation errors (5.1) by each method with respect to the wall time. The means of the 10 simulations are shown as solid lines and the shaded areas correspond to one standard deviation away from the mean. It is seen that Vanilla-FNN yields a rapid decay in the extrapolation error during the initial phase, however, it saturates quickly and progresses marginally as the training goes on. It can be seen that TA-ROM yields the largest variance in the extrapolation error. This is because of their unstable behavior in the training. Note that for TA-ROM, the test error is available only after the SAE training is complete. On the other hand, tLaSDI gives the smallest extrapolation errors for all 10 simulations and yields the smallest variance. This indicates the robust prediction ability of tLaSDI in extrapolation.

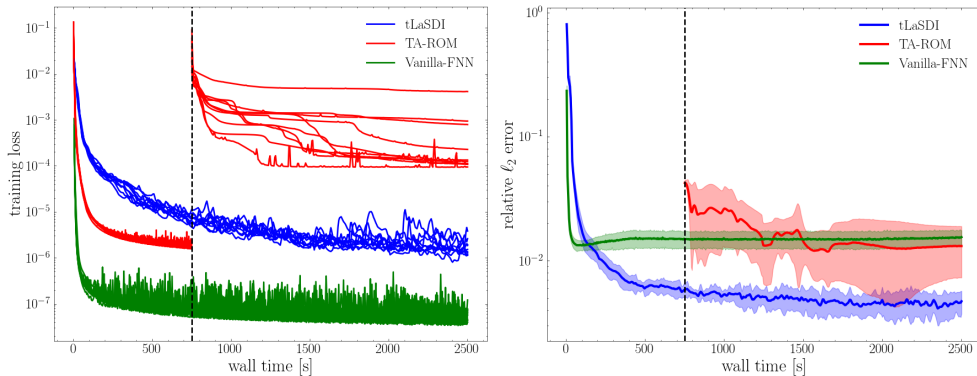


Fig. 2: Example 5.1.1. Left: The training loss trajectories for 10 simulations versus the wall time by the three methods. Right: The mean and one standard deviation away from the mean of the extrapolation errors (5.1) versus the wall time. The vertical line indicates the time for TA-ROM trains SAE.

In practice, the training loss is perhaps the only indicator for the users to decide whether the model is well-trained or not. Without additional information, one may choose the model that yields the smallest loss if multiple simulations are done. In Figure 3, we depict the prediction trajectories (extrapolation region) from the model with the smallest training loss among 10 simulations. The corresponding ground truth (GT) trajectories are shown in black dashed lines. It is clearly observed that tLaSDI

provides the most accurate extrapolation performance despite it being a non-intrusive ROM method. The extrapolation errors by tLaSDI, TA-ROM, and Vanilla-FNN are 3.65×10^{-3} , 1.36×10^{-2} and 1.04×10^{-2} , respectively.

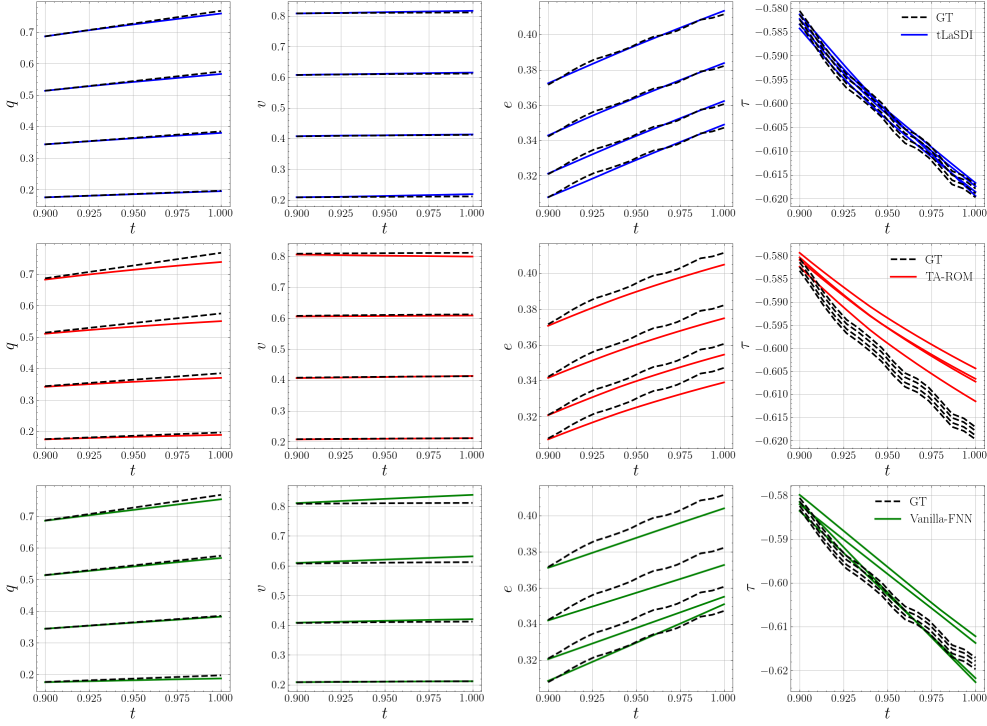


Fig. 3: Example 5.1.1. Four different GT trajectories and the corresponding predictions by tLaSDI (top row), TA-ROM (middle row), and Vanilla-FNN (bottom row). Each method uses the model with the smallest loss from 10 independent simulations.

5.1.2 Two gas containers exchanging heat and volume

Two ideal gas containers, separated by a wall, are allowed to exchange heat and volume. The dynamics of the wall are described by four variables: position (q) and momentum (p) of the moving wall, and the entropy of the gases in the two containers, (S_1 , S_2). The evolution of the variables is then modeled by

$$\begin{pmatrix} \dot{q} \\ \dot{p} \\ \dot{S}_1 \\ \dot{S}_2 \end{pmatrix} = \begin{pmatrix} p \\ \frac{2}{3} \left(\frac{E_1}{q} - \frac{E_2}{2-q} \right) \\ \frac{10}{T_1} \left(\frac{1}{T_1} - \frac{1}{T_2} \right) \\ -\frac{10}{T_1} \left(\frac{1}{T_1} - \frac{1}{T_2} \right) \end{pmatrix}, \quad E_j = \frac{\exp\left(\frac{2S_j}{3}\right)}{(q + 2(j-1)(1-q))^{2/3}},$$

where $T_j = \frac{\partial E_j}{\partial S_j}$, E_1 and E_2 are the internal energy of the two containers given by [49]. This example is also considered in [26, 29, 50].

Following [33], we generate 100 trajectories of different initial conditions that are randomly uniformly sampled from $[0.2, 1.8] \times [-1, 1] \times [1, 3] \times [1, 3]$. If the variables for i -th trajectory are denoted by q_i , p_i , $S_{1,i}$, and $S_{2,i}$, we construct the full-state variable \mathbf{x} by concatenating them all, i.e., $\mathbf{x}(t) = [\mathbf{q}(t), \mathbf{p}(t), \mathbf{S}_1(t), \mathbf{S}_2(t)]^\top \in \mathbb{R}^{400}$, where $\mathbf{q} = (q_i)$, $\mathbf{p} = (p_i)$, $\mathbf{S}_1 = (S_{1,i})$ and $\mathbf{S}_2 = (S_{2,i})$. Hence, the full-order dimension is $N = 400$. We set $T = 7.84$, $\delta = 0.16$ with the fixed time step of $\Delta t = 0.02$.

In all the methods, we employ the autoencoders having $207K$ parameters with the latent space dimension of $n = 30$. The numbers of parameters for the latent space dynamics of Vanilla-FNN, TA-ROM, and tLaSDI are $910K$, $870K$, and $900K$ respectively. The training of all models is terminated after about 10K seconds of wall-clock time, which amounts to approximately $70K$ and $800K$ iterations for tLaSDI and Vanilla-FNN respectively. For TA-ROM, the training involves $440K$ and $160K$ iterations for SAE and SPNN respectively, leading to a total of $600K$ iterations. The number of iterations for SAE and SPNN of TA-ROM is meticulously chosen regarding the extrapolation performance. Other implementation details can be found in Appendix B.2.

Figure 4 shows the training loss and extrapolation error trajectories by the three methods with respect to the wall-clock time in seconds. We run 10 independent simulations and report all the training loss trajectories on the left. Similarly as before, we see a clear separation of the loss between the three methods because of the different scales of the training loss functions. Yet, all the methods reach to some saturated levels at the end of the training. On the right, we report the extrapolation errors (5.1) with respect to the wall time. The means of the 10 simulations are shown as solid lines and the shaded areas are one standard deviation away from the mean. Again, it is clearly observed that tLaSDI yields not only the smallest extrapolation error but also the smallest variance overall, especially toward the end of the training. This again illustrates the effectiveness of tLaSDI in extrapolation.

In addition, we report some prediction trajectories (extrapolation regions) in Figure 3. The trajectories are generated from the model that achieves the smallest loss among 10 independent simulations. The black dashed lines represent the corresponding GT trajectories. Again, it is clearly seen that tLaSDI exhibits robust extrapolation capability, especially for the position q (first column) and the momentum p (second column). In contrast, TA-ROM and Vanilla-FNN yield incorrect trajectories for q and p , which are typical behaviors of the non-intrusive approaches. The extrapolation errors by tLaSDI, TA-ROM, and Vanilla-FNN are 3.88×10^{-3} , 2.57×10^{-2} and 2.09×10^{-2} , respectively.

5.2 Parametric PDEs

For parametric PDE examples, we are interested in capturing a distinct behavior of the solution over time, and at the same time, in achieving accurate predictions on unseen parameters. In this regard, the prediction error at a given parameter μ is measured

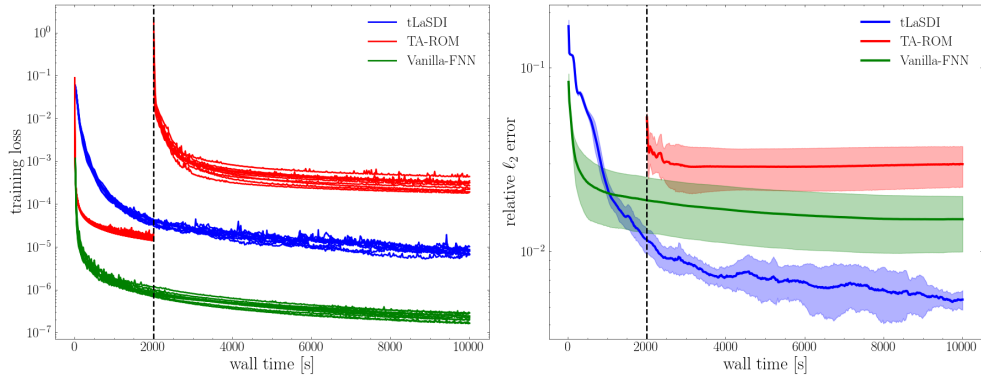


Fig. 4: Example 5.1.2. Left: The training loss trajectories for 10 simulations versus the wall time by the three methods. Right: The mean and one standard deviation away from the mean of the extrapolation errors (5.1) versus the wall time. The vertical line indicates the time for TA-ROM trains SAE.

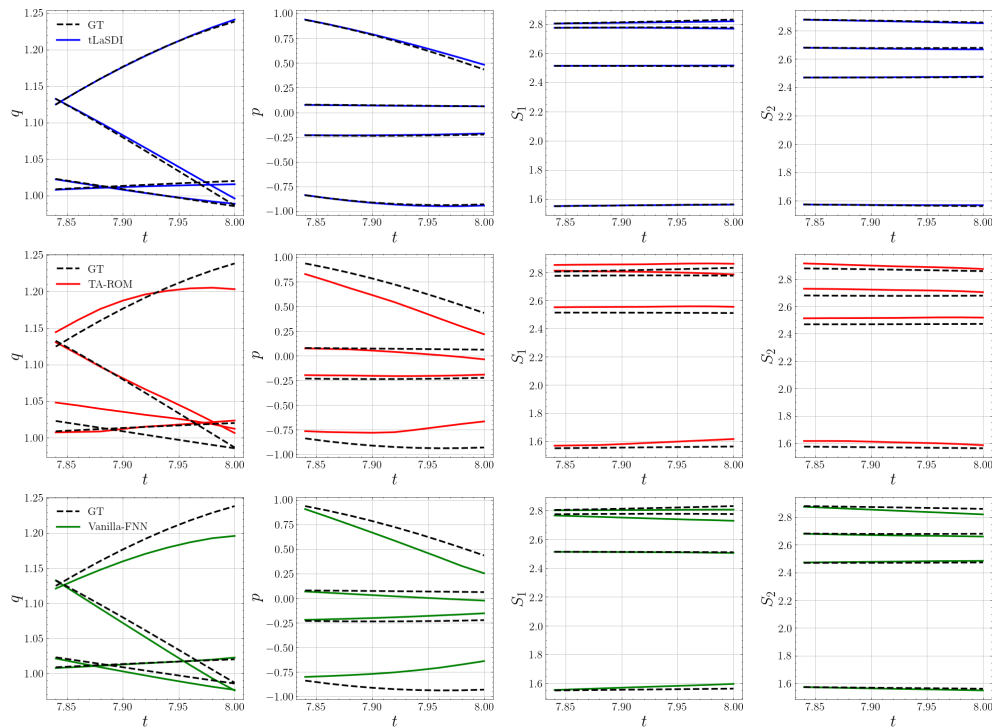


Fig. 5: Example 5.1.2: Four different GT trajectories and the corresponding predictions by tLaSDI (top row), TA-ROM (middle row), and Vanilla-FNN (bottom row). Each method uses the model with the smallest loss from 10 independent simulations.

by the maximum percentage relative ℓ_2 error over time, i.e.,

$$e_\mu^{\max\%} = 100 \times \max_k \frac{\|\mathbf{x}_\mu^k - \tilde{\mathbf{x}}_\mu^k\|_2}{\|\mathbf{x}_\mu^k\|_2}. \quad (5.2)$$

Let $u_\mu(x, t)$ be the solution to a parametric PDE. The full state variable \mathbf{x}_μ^k then corresponds to the collection of the solution at time t_k evaluated at N grid points $\{x_j\}_{j=1}^N$. That is, $\mathbf{x}_\mu^k = (u_\mu(x_j, t_k))_j \in \mathbb{R}^N$.

To ensure high prediction accuracy, the training data \mathbf{x}_μ^k need to be collected at carefully selected parameters, which are often referred to as training parameters or training samples. In this regard, we employ the greedy sampling algorithm proposed in [18] for training data generation. The greedy sampling utilizes a physics-informed residual-based error indicator to select proper training parameters from Ω_μ , during training. Training data is produced on-the-fly at the sampled parameters during the training process. The greedy sampling is known to outperform the traditional pre-determined uniform (equidistant) sampling in terms of prediction accuracy [18]. We remark that the greedy sampling method may yield distinct training parameter selections for different ROM models. The implementation details of greedy sampling for the following examples can be found in Appendix B.3.

We compare tLaSDI with another nonlinear manifold ROM, gLaSDI [18] that proposed the aforementioned greedy sampling algorithm. gLaSDI uses a user-defined library of candidate basis functions (e.g., polynomials, trigonometric functions) to represent the latent space dynamics. A brief overview of gLaSDI can be found in Appendix A.

5.2.1 1D Burgers' equation

We consider the 1D parametric inviscid Burgers' equation, which serves as a simplified model to exhibit the formation of shock waves in fluid dynamics and nonlinear acoustics. The parametric PDE under consideration reads

$$\begin{aligned} \frac{\partial u_\mu}{\partial t} + u \frac{\partial u_\mu}{\partial x} &= 0, \quad \forall (x, t) \in (-3, 3) \times (0, 2], \\ u_\mu(3, t) &= u_\mu(-3, t), \quad \forall t \in (0, 2] \\ u_\mu(x, 0) &= \alpha \exp\left(-\frac{x^2}{2\omega^2}\right), \quad \forall x \in (-3, 3), \end{aligned} \quad (5.3)$$

where the initial condition is parametrized by the amplitude α , and the width ω . Let $\mu = (\alpha, \omega)$ and the parameter domain be $\Omega_\mu = [0.7, 0.8] \times [0.9, 1.0]$. Both parameters ω and α are discretized into 21 evenly spaced points within their respective ranges. This discretization yields a set of 441 distinct parameters in the parameter domain. The training data are discretized with the spatial and time spacing $\Delta x = 6/200$, $\Delta t = 2/200$. Consequently, the dimension of the full-order model is $N = 201$. We collect 25 training data at the parameters selected using the greedy sampling algorithm, during training. At the end of the training, tLaSDI and gLaSDI generated distinct sets of training data. Additional details on implementation are provided in Appendix B.3.

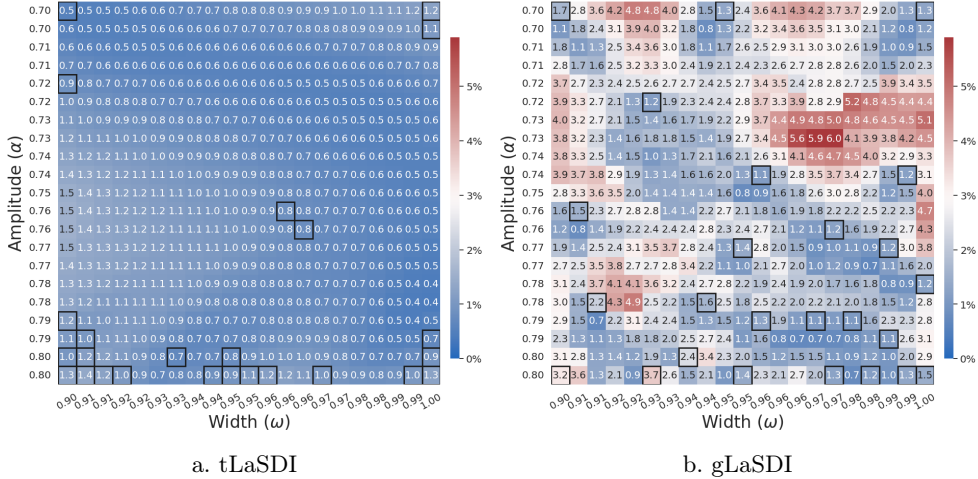


Fig. 6: Example 5.2.1. Comparison between tLaSDI and gLaSDI [18]. The number on each box represents the maximum percentage relative error (5.2) computed at each parameter. The black square boxes denote the positions of the sampled training points.

The latent dimension is set to $n = 10$. The total number of parameters for hyper-autoencoder and GFINNs in tLaSDI are approximately 905K and 35K respectively. tLaSDI is trained by Adam optimizer [48] for 42K iterations.

The heatmaps of the maximum percentage relative ℓ_2 errors (5.2) of tLaSDI and gLaSDI computed at all 441 parameters are depicted in Figure 6. The black square boxes indicate the training parameters sampled using the greedy sampling algorithm. It is observed that the sampled parameters for tLaSDI tend to cluster near the boundaries, while no notable pattern is observed for gLaSDI. In terms of accuracy, tLaSDI and gLaSDI give the worst-case errors of 1.5% and 6.0%, respectively, among 441 parameters.

tLaSDI constructs a thermodynamic structure in the latent dynamics which provides the NN-based entropy function S_{NN} in the latent space. Figure 6 shows the data-driven entropy function and its rate of change with respect to time. The mean over all the test parameters is reported and the shared area is one standard deviation away from the mean. As promised by GFINNs, we see that the entropy is increasing as the rate is always non-negative. The entropy production rate $\frac{d}{dt} S_{\text{NN}}(z(t))$ has the largest value at the final time $t = 2$, which happens to be the time where the full-state solution exhibits the stiffest pattern. See the right of Figure 6 for the tLaSDI prediction at varying times.

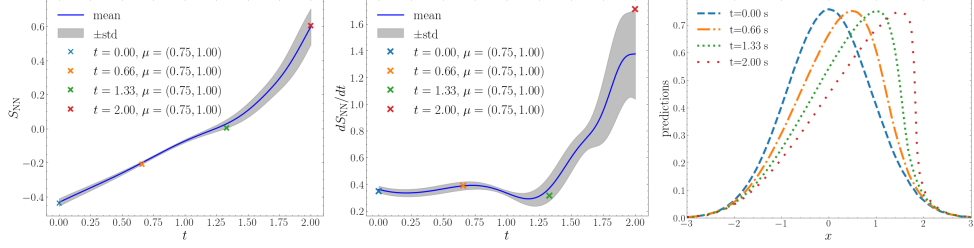


Fig. 7: Example 5.2.1. The mean and one standard deviation away from the mean of (left) the entropy S_{NN} and (middle) $\frac{d}{dt}S_{\text{NN}}$ across the test parameters. Right: The solution prediction by tLaSDI at the four times at $\mu = (0.75, 1.00)$ whose corresponding S_{NN} and $\frac{d}{dt}S_{\text{NN}}$ are marked in the left and middle figures.

5.2.2 1D heat equation

To further investigate the correlation captured by the data-driven entropy from tLaSDI, we consider the following parametric heat equation:

$$\frac{\partial u_\mu}{\partial t} - \frac{\partial^2 u_\mu}{\partial x^2} = 0, \quad \forall (x, t) \in (-3, 3) \times (0, 2],$$

with the same boundary and initial conditions to the Burgers' equation (5.3). We follow the same setup as the earlier example and report the details in Appendix B.3.

In Figure 8, we report the graphs of the data-driven entropy from tLaSDI and its rate along with the tLaSDI prediction at varying times. In contrast with the Burgers equation, it is clearly observed that the entropy production rate $\frac{d}{dt}S_{\text{NN}}(z(t))$ decreases over time, reflecting the diffusive behavior of the solution to the heat equation. This comparison illustrates a distinct feature of tLaSDI through the data-driven entropy which exhibits a strong correlation with the underlying physical processes.

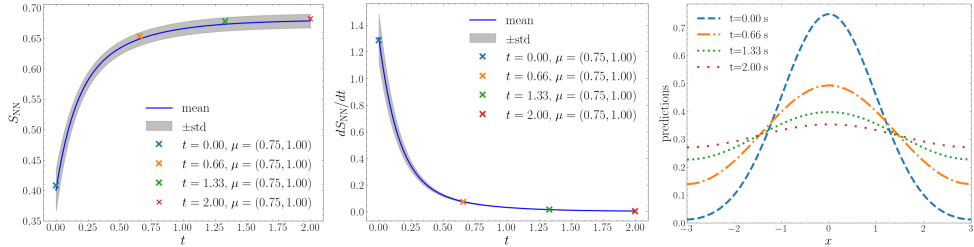


Fig. 8: Example 5.2.2. The mean and one standard deviation away from the mean of (left) the entropy S_{NN} and (middle) $\frac{d}{dt}S_{\text{NN}}$ across the test parameters. Right: The solution prediction by tLaSDI at the four times at $\mu = (0.75, 1.00)$ whose corresponding S_{NN} and $\frac{d}{dt}S_{\text{NN}}$ are marked in the left and middle figures.

6 Conclusions

We propose a non-intrusive thermodynamics-informed ROM method, namely, tLaSDI. tLaSDI uses an autoencoder to construct a nonlinear manifold as the latent space and models the latent dynamics through GFINNs. GFINNs are structured to precisely satisfy the GENERIC formalism which ensures the exact fulfillment of the first and second laws of thermodynamics. Based on an abstract error estimate of ROM approximation, a new loss is formulated, which significantly improves the performance of tLaSDI. Numerical examples are presented to demonstrate the effectiveness of tLaSDI. For the data-driven discovery tasks, tLaSDI exhibits robust extrapolation ability, which typical pure data-driven approaches lack. For the parametric PDE problems, we found that tLaSDI provides smaller prediction errors on unseen parameters when it is compared with gLaSDI. Due to the thermodynamic infusion, tLaSDI returns the data-driven entropy function defined in the latent space. We found that this entropy function from tLaSDI captures not only the time on which the solution to the Burgers' equation is the stiffest but also the time on which the solution to the heat equation is the most diffusive through the entropy production rate.

Acknowledgements. J. S. R. Park was partially supported by Miwon Du-Myeong Fellowship via Miwon Commercial Co., Ltd. and a KIAS Individual Grant (AP095601) via the Center for AI and Natural Sciences at Korea Institute for Advanced Study. S. W. Cheung and Y. Choi were partially supported for this work by Laboratory Directed Research and Development (LDRD) Program by the U.S. Department of Energy (24-ERD-035). Y. Choi was partially supported for this work by the U.S. Department of Energy, Office of Science, Office of Advanced Scientific Computing Research, as part of the CHaRMNET Mathematical Multifaceted Integrated Capability Center (MMICC) program, under Award Number DE-SC0023164 at Lawrence Livermore National Laboratory. Y. Shin was partially supported for this work by the NRF grant funded by the Ministry of Science and ICT of Korea (RS-2023-00219980). Lawrence Livermore National Laboratory is operated by Lawrence Livermore National Security, LLC, for the U.S. Department of Energy, National Nuclear Security Administration under Contract DE-AC52-07NA27344. IM release number: LLNL-JRNL-860848.

Appendix A An overview of existing methods

In this section, we provide a brief overview of the existing nonlinear manifold ROM methods.

Vanilla-FNN: This algorithm leverages the standard feed-forward neural network (FNN) for both autoencoder and latent space dynamics. It employs a loss function composed of two standard components, integration loss \mathcal{L}_{int} and reconstruction loss \mathcal{L}_{rec} . The autoencoder and the latent space dynamics (FNN) are trained simultaneously within this algorithm.

TA-ROM (Thermodynamics-aware reduced-order models [33]): In this algorithm, the sparse autoencoder (SAE) [51] is utilized for the dimension reduction. The SPNN [42] is employed to embed the GENERIC formalism into latent space dynamics. In this framework, they train SAE first, and then SPNN subsequently. The training procedure utilizes the following loss formulation

$$\begin{aligned}\mathcal{L}_{\text{SAE}} &= \mathcal{L}_{\text{rec}} + \lambda_{\text{spr}}\mathcal{L}_{\text{spr}}, \\ \mathcal{L}_{\text{SPNN}} &= \lambda_{\text{int}}\mathcal{L}_{\text{int}} + \mathcal{L}_{\text{deg}},\end{aligned}$$

in addition to the standard ℓ_2 regularization for the weight decay of SPNN. In this framework, the dimension of latent space is not predetermined. It is rather discovered by minimizing the sparsity loss \mathcal{L}_{spr} [33, 51] during SAE training to eliminate insignificant components of the latent vector. The degeneracy condition of GENERIC formalism is not exactly satisfied with SPNN. Instead, it is enforced through the minimization of the degeneracy loss component \mathcal{L}_{deg} :

$$\mathcal{L}_{\text{deg}} = \sum_k (\|L_{NN}\nabla S_{NN}\|_2^2 + \|M_{NN}\nabla E_{NN}\|_2^2),$$

where the neural networks are evaluated at $\phi_e(\mathbf{x}^k)$.

gLaSDI (Parametric physics-informed greedy latent space dynamics identification [18]): This algorithm is developed for ROM of high-dimensional parametric dynamical systems. Its primary distinction from our proposed method lies in the latent space dynamics identification (DI) model. In gLaSDI, the latent space dynamics F_μ^r are identified using a user-defined library of candidate basis functions (e.g., polynomial, trigonometric, exponential functions) at each training parameter. To enable the identification of latent dynamics beyond the training parameters, the k -nearest neighbors (KNN) convex interpolation is utilized. The algorithm uses a greedy sampling strategy based on a physics-informed residual-based error indicator to select training parameters during the training process. The goal of greedy sampling is to efficiently generate training data on-the-fly that yield optimal prediction performance. In this framework, the autoencoder and the DI model are trained simultaneously minimizing the loss function $\mathcal{L}_{\text{gLaSDI}} = \mathcal{L}_{\text{rec}} + \lambda_{\text{mod}}\mathcal{L}_{\text{mod}}$.

The comparison of tLaSDI with TA-ROM and Vanilla-FNN is introduced in Table A1. While specific DI models are proposed by default within each framework, it is worth noting that tLaSDI and TA-ROM are compatible with both GFNNs and SPNN.

However, for simplicity, the numerical results presented in this work adhere to the conventional pairings: tLaSDI with GFINNs and TA-ROM with SPNN.

Method	DI model	Loss components	Training AE/DI model
tLaSDI	GFINNs	$\mathcal{L}_{\text{int}}, \mathcal{L}_{\text{rec}}, \mathcal{L}_{\text{Jac}}, \mathcal{L}_{\text{mod}}$	Simultaneous
TA-ROM	SPNN	$\mathcal{L}_{\text{int}}, \mathcal{L}_{\text{rec}}, \mathcal{L}_{\text{spr}}, \mathcal{L}_{\text{deg}}$	Separate
Vanilla	FNN	$\mathcal{L}_{\text{int}}, \mathcal{L}_{\text{rec}}$	Simultaneous
gLaSDI	Dictionary	$\mathcal{L}_{\text{rec}}, \mathcal{L}_{\text{mod}}$	Simultaneous

Table A1: Comparative overview of tLaSDI and other methods

Appendix B Implementation details

In this appendix, we outline the implementation details, including training data generation and hyperparameter settings for the ROM models implemented in all numerical examples in Section 5.

B.1 Couette flow of an Oldroyd-B fluid

This section introduces the implementation details of tLaSDI, TA-ROM, and Vanilla-FNN for the results presented in Section 5.1.1.

The training database is provided by the authors of [33]. This database was generated with MATLAB employing a multiscale approach in the dimensionless form outlined in [52, Section 5.6]. The derivative data are obtained from the training data using the central difference approximation scheme. At the endpoints, $t = 0$ and $t = T$, where the central difference scheme is not feasible, forward and backward difference schemes were employed, respectively.

The TA-ROM was implemented referring to the training details presented in [33] and the associated source code¹. Table B2 lists the loss weights assigned to the loss components of each method. Additionally, the standard ℓ_2 regularization is implemented for the weight decay of DI models. The regularization weights are set at $\lambda_{\text{reg}} = 10^{-8}$ for tLaSDI, Vanilla-FNN and $\lambda_{\text{reg}} = 10^{-5}$ for TA-ROM. Table B3 presents other main hyperparameters used for the training of tLaSDI, TA-ROM and Vanilla-FNN. The hyperparameters are carefully chosen to optimize the performance of each method. The training of all methods is based on a full batch of training data. The Runge-Kutta-Fehlberg method (RK45) is utilized for the time-step integration of latent space dynamics during the training and prediction stages of all models.

B.2 Two gas containers exchanging heat and volume

The implementation details of tLaSDI, TA-ROM, and Vanilla-FNN, pertaining to the results presented in Section 5.1.2, are presented in this section.

The training snapshots were generated by the Runge-Kutta-Fehlberg method (RK45) based on the source code² from the original GFINNs study [29]. The

¹GitHub page: <https://github.com/quercushernandez/DeepLearningMOR>

²GitHub page: https://github.com/zzhang222/gfinn_gc/tree/main

Method	λ_{int}	λ_{rec}	λ_{Jac}	λ_{mod}	λ_{deg}	λ_{spr}
tLaSDI	1	1e-1	1e-2	1e-8	N/A	N/A
TA-ROM	1e+3	1	N/A	N/A	1	1e-4
Vanilla-FNN	1	1e-1	N/A	N/A	N/A	N/A

Table B2: Example 5.1.1: Loss weights used for implementations of tLaSDI, TA-ROM, and Vanilla-FNN

GFINNs				
NN layers	NN width	activation f	optimizer	learning rate
5	100	tanh	Adam	1e-4
Autoencoder				
Architecture		activation f	optimizer	learning rate
400-160-160-8		ReLU	Adam	1e-4

(a) tLaSDI

SPNN				
NN layers	NN width	activation f	optimizer	learning rate
5	100	tanh	Adam	1e-5
Autoencoder				
Architecture		activation f	optimizer	learning rate
400-160-160-8		ReLU	Adam	1e-5

(b) TA-ROM

FNN				
NN layers	NN width	activation f	optimizer	learning rate
5	215	tanh	Adam	1e-4
Autoencoder				
Architecture		activation f	optimizer	learning rate
400-160-160-8		ReLU	Adam	1e-4

(c) Vanilla-FNN

Table B3: Hyperparameters used for Example 5.1.1: All NNs within GFINNs and SPNN adhere to the hyperparameters specified in this table. The architecture of FNN in Vanilla-FNN was chosen to have the same level of number of parameters as GFINNs in tLaSDI. As the encoder and decoder architectures are symmetric, we refer to the architecture of the encoder to represent that of the autoencoder for simplicity.

corresponding derivative data were obtained by applying the central difference approximation scheme to the training snapshots. At the endpoints $t = 0$ and $t = T$, where the central difference scheme is not applicable, we employed forward and backward difference schemes, respectively.

The loss weights allocated to the respective loss components for both methods are outlined in Table B4. For the implementation of TA-ROM, we adopted standard ℓ_2 regularization for the weight decay of SPNN, setting the regularization weight at $\lambda_{\text{reg}} = 10^{-5}$. For the TA-ROM implementation, we referred to the training details in

[33] and its associated code³. The hyperparameters of each method have been meticulously fine-tuned to achieve optimal performance. Table B5 lists the other principal hyperparameters used for the training of tLaSDI, TA-ROM, and Vanilla-FNN. All methods employ the full batch of training data during their training processes. The initial learning rates are listed in the table, and they undergo decay after every 1000 iterations until they reach 10^{-5} . The decay rates are set to 1% for tLaSDI and Vanilla-FNN and 5% for TA-ROM for both autoencoders and DI models. The Runge-Kutta second/third order integrator (RK23) is employed for temporal integration of latent dynamics for all methods.

Method	λ_{int}	λ_{rec}	λ_{Jac}	λ_{mod}	λ_{deg}	λ_{spr}
tLaSDI	1	1e-1	1e-2	1e-7	N/A	N/A
TA-ROM	1e+3	1	N/A	N/A	1	1e-4
Vanilla-FNN	1	1e-1	N/A	N/A	N/A	N/A

Table B4: Example 5.1.2: Loss weights used for implementations of tLaSDI, TA-ROM, and Vanilla-FNN

B.3 1D Burgers equation

The implementation details for the tLaSDI and gLaSDI [18] corresponding to the results in Section 5.2.1, are presented in this section.

The greedy sampling algorithm in our implementations operates as follows: The training initiates with four initial data points collected at the corners of the parameter domain, $(0.7, 0.9)$, $(0.7, 1.0)$, $(0.8, 0.9)$, $(0.8, 1.0)$. After every 2,000 epochs, a new parameter that maximizes a physics-informed residual-based error is selected. At this newly identified parameter, a high-fidelity simulation is executed to solve equation (5.3), and the resulting solution is added to the training dataset. This process is repeated until the dataset encompasses 25 training samples, including the initial four. For more detailed insights into each step, refer to [18].

We initially generate solution data with uniform spatial and time steps of $\Delta x = 6/1000$ and $\Delta t = 2/1000$, respectively. The solution data were generated using an implicit Euler time integration method, while the corresponding derivatives were calculated using a backward difference scheme. From this dataset, the training data and the corresponding derivatives are subsampled with the resolution of $\Delta x = 6/200$ and $\Delta t = 2/200$.

For the gLaSDI implementation, we closely followed the algorithm detailed in [18], utilizing the code⁴ provided by the authors. The following loss functions are used for tLaSDI and gLaSDI.

$$\begin{aligned} \text{tLaSDI} : \mathcal{L}_{\text{int}} + 10^{-1}\mathcal{L}_{\text{rec}} + 10^{-9}\mathcal{L}_{\text{Jac}} + 10^{-7}\mathcal{L}_{\text{mod}} \\ \text{gLaSDI} : \mathcal{L}_{\text{rec}} + \mathcal{L}_{\text{mod}} \end{aligned}$$

³GitHub page: <https://github.com/quercushernandez/DeepLearningMOR>

⁴GitHub page: <https://github.com/LLNL/gLaSDI>

GFINNs				
NN layers	NN width	activation f	optimizer	learning rate
5	200	sine	Adam	1e-4
Autoencoder				
Architecture	activation f	optimizer	learning rate	
400-200-100-30	ReLU	Adam	1e-4	

(a) tLaSDI

SPNN				
NN layers	NN width	activation f	optimizer	learning rate
5	200	sine	Adam	1e-4
Autoencoder				
Architecture	activation f	optimizer	learning rate	
400-200-100-30	ReLU	Adam	1e-4	

(b) TA-ROM

FNN				
NN layers	NN width	activation f	optimizer	learning rate
5	540	sine	Adam	1e-4
Autoencoder				
Architecture	activation f	optimizer	learning rate	
400-200-100-30	ReLU	Adam	1e-4	

(c) Vanilla-FNN

Table B5: Hyperparameters used for Example 5.1.2: All NNs within GFINNs and SPNN adhere to the hyperparameters specified in this table. The architecture of FNN in Vanilla-FNN was chosen to have the same level of number of parameters as GFINNs in tLaSDI. As the encoder and decoder architectures are symmetric, we refer to the architecture of the encoder to represent that of the autoencoder for simplicity.

Other main hyperparameters used to train tLaSDI and gLaSDI are reported in Table B6. The hyperparameters are selected to yield optimal predictive performance of each method. The initial learning rates are listed in the table. The learning rate decay is conducted for both autoencoder and GFINNs in tLaSDI after every 1000 epochs with a 1% decay rate. The batch size was adjusted so that the number of batches is 4 for tLaSDI and 2 for gLaSDI. The Runge-Kutta-Fehlberg method (RK23) is employed for the time-step integration of latent dynamics for tLaSDI. The time integration of latent dynamics for gLaSDI is conducted using an ODE solver, odeint function of the Scipy library [53].

Further specification of hyperparameters is required for gLaSDI. A quadratic polynomial is employed in the dictionary-based DI model. The KNN convex interpolation scheme utilizes 1 and 5 nearest neighbors to evaluate the model beyond the training parameters during greedy sampling and prediction, respectively. For a more comprehensive understanding of these hyperparameters, readers are referred to [18].

GFINNs				
NN layers	NN width	activation f	optimizer	learning rate
5	40	tanh	Adam	1e-4
Autoencoder				
Architecture	activation f	optimizer	learning rate	
201-100-10	ReLU	-	-	
Hypernetworks				
NN layers	NN width	activation f	optimizer	learning rate
3	20	tanh	Adam	1e-4

(a) tLaSDI

Autoencoder			
Architecture	activation f	optimizer	learning rate
201-100-10	Sigmoid	Adam	1e-3

(b) gLaSDI

Table B6: Hyperparameters used for Example 5.2.1: All NNs within the GFINNs model adhere to the same hyperparameters specified in this table. As the encoder and decoder architectures are symmetric, we refer to the architecture of the encoder to represent that of the autoencoder for simplicity. We note that the network parameters of autoencoder are not directly trainable, rather, they are optimized through the training of hypernetworks.

References

- [1] Bongard, J., Lipson, H.: Automated reverse engineering of nonlinear dynamical systems. *Proceedings of the National Academy of Sciences* **104**(24), 9943–9948 (2007)
- [2] Schmidt, M., Lipson, H.: Distilling free-form natural laws from experimental data. *science* **324**(5923), 81–85 (2009)
- [3] Brunton, S.L., Proctor, J.L., Kutz, J.N.: Discovering governing equations from data by sparse identification of nonlinear dynamical systems. *Proceedings of the national academy of sciences* **113**(15), 3932–3937 (2016)
- [4] Raissi, M., Karniadakis, G.E.: Hidden physics models: Machine learning of nonlinear partial differential equations. *Journal of Computational Physics* **357**, 125–141 (2018)
- [5] Wu, K., Xiu, D.: Data-driven deep learning of partial differential equations in modal space. *Journal of Computational Physics* **408**, 109307 (2020)
- [6] Xiao, D., Fang, F., Buchan, A.G., Pain, C.C., Navon, I.M., Du, J., Hu, G.: Non-linear model reduction for the Navier–Stokes equations using residual DEIM method. *Journal of Computational Physics* **263**, 1–18 (2014)
- [7] Burkardt, J., Gunzburger, M., Lee, H.-C.: POD and CVT-based reduced-order modeling of Navier–Stokes flows. *Computer Methods in Applied Mechanics and Engineering* **196**(1-3), 337–355 (2006)
- [8] Choi, Y., Carlberg, K.: Space–time least-squares Petrov–Galerkin projection for nonlinear model reduction. *SIAM Journal on Scientific Computing* **41**(1), 26–58 (2019)
- [9] Choi, Y., Coombs, D., Anderson, R.: SNS: a solution-based nonlinear subspace method for time-dependent model order reduction. *SIAM Journal on Scientific Computing* **42**(2), 1116–1146 (2020)
- [10] Carlberg, K., Choi, Y., Sargsyan, S.: Conservative model reduction for finite-volume models. *Journal of Computational Physics* **371**, 280–314 (2018)
- [11] Copeland, D.M., Cheung, S.W., Huynh, K., Choi, Y.: Reduced order models for lagrangian hydrodynamics. *Computer Methods in Applied Mechanics and Engineering* **388**, 114259 (2022)
- [12] Cheung, S.W., Choi, Y., Copeland, D.M., Huynh, K.: Local lagrangian reduced-order modeling for rayleigh-taylor instability by solution manifold decomposition. preprint arXiv:2201.07335 (2022)
- [13] Zhao, P., Liu, C., Feng, X.: POD-DEIM based model order reduction for the

- spherical shallow water equations with Turkel-Zwas finite difference discretization. *Journal of Applied Mathematics* (2014)
- [14] Stefanescu, R., Navon, I.M.: POD/DEIM nonlinear model order reduction of an advection implicit shallow water equations model. *Journal of Computational Physics* **237**, 95–114 (2013)
- [15] Choi, Y., Brown, P., Arrighi, B., Anderson, R., Huynh, K.: Space-time reduced order model for large-scale linear dynamical systems with application to Boltzmann transport problems. *Journal of Computational Physics* **424**, 109845 (2021)
- [16] Schmid, P.J.: Dynamic mode decomposition of numerical and experimental data. *Journal of fluid mechanics* **656**, 5–28 (2010)
- [17] Fries, W.D., He, X., Choi, Y.: LaSDI: Parametric latent space dynamics identification. *Computer Methods in Applied Mechanics and Engineering* **399**, 115436 (2022)
- [18] He, X., Choi, Y., Fries, W.D., Belof, J.L., Chen, J.-S.: gLaSDI: Parametric physics-informed greedy latent space dynamics identification. *Journal of Computational Physics*, 112267 (2023)
- [19] Bonneville, C., Choi, Y., Ghosh, D., Belof, J.L.: GPLaSDI: Gaussian process-based interpretable latent space dynamics identification through deep autoencoder. *Computer Methods in Applied Mechanics and Engineering* **418**, 116535 (2024)
- [20] Lee, K., Carlberg, K.T.: Model reduction of dynamical systems on nonlinear manifolds using deep convolutional autoencoders. *Journal of Computational Physics* **404**, 108973 (2020)
- [21] Lee, K., Carlberg, K.T.: Deep conservation: A latent-dynamics model for exact satisfaction of physical conservation laws. In: *Proceedings of the AAAI Conference on Artificial Intelligence*, vol. 35, pp. 277–285 (2021)
- [22] Kim, Y., Choi, Y., Widemann, D., Zohdi, T.: Efficient nonlinear manifold reduced order model. preprint arXiv:2011.07727 (2020)
- [23] Kim, Y., Choi, Y., Widemann, D., Zohdi, T.: A fast and accurate physics-informed neural network reduced order model with shallow masked autoencoder. *Journal of Computational Physics*, 110841 (2022)
- [24] Grmela, M., Öttinger, H.C.: Dynamics and thermodynamics of complex fluids. i. development of a general formalism. *Physical Review E* **56**(6), 6620 (1997)
- [25] Öttinger, H.C., Grmela, M.: Dynamics and thermodynamics of complex fluids. ii. illustrations of a general formalism. *Physical Review E* **56**(6), 6633 (1997)

- [26] Öttinger, H.C.: Beyond Equilibrium Thermodynamics. John Wiley & Sons, Hoboken, NJ (2005)
- [27] DeMers, D., Cottrell, G.: Non-linear dimensionality reduction. *Advances in neural information processing systems* **5** (1992)
- [28] Hinton, G.E., Salakhutdinov, R.R.: Reducing the dimensionality of data with neural networks. *science* **313**(5786), 504–507 (2006)
- [29] Zhang, Z., Shin, Y., Karniadakis, G.E.: GFINNs: Generic formalism informed neural networks for deterministic and stochastic dynamical systems. *Philosophical Transactions of the Royal Society A* **380**(2229), 20210207 (2022)
- [30] Öttinger, H.C.: Preservation of thermodynamic structure in model reduction. *Physical Review E* **91**(3), 032147 (2015)
- [31] Yu, H., Tian, X., Weinan, E., Li, Q.: Onsagernet: Learning stable and interpretable dynamics using a generalized onsager principle. *Physical Review Fluids* **6**(11), 114402 (2021)
- [32] Chen, X., Soh, B.W., Ooi, Z.-E., Vissol-Gaudin, E., Yu, H., Novoselov, K.S., Hip-palgaonkar, K., Li, Q.: Constructing custom thermodynamics using deep learning. *Nature Computational Science*, 1–20 (2023)
- [33] Hernandez, Q., Badias, A., Gonzalez, D., Chinesta, F., Cueto, E.: Deep learning of thermodynamics-aware reduced-order models from data. *Computer Methods in Applied Mechanics and Engineering* **379**, 113763 (2021)
- [34] Moya, B., Badias, A., Gonzalez, D., Chinesta, F., Cueto, E.: Physics perception in sloshing scenes with guaranteed thermodynamic consistency. *IEEE Transactions on Pattern Analysis and Machine Intelligence* **45**(2), 2136–2150 (2022)
- [35] Masi, F., Stefanou, I.: Multiscale modeling of inelastic materials with thermodynamics-based artificial neural networks (tann). *Computer Methods in Applied Mechanics and Engineering* **398**, 115190 (2022)
- [36] Champion, K., Lusch, B., Kutz, J.N., Brunton, S.L.: Data-driven discovery of coordinates and governing equations. *Proceedings of the National Academy of Sciences* **116**(45), 22445–22451 (2019)
- [37] Vijayarangan, V., Uranakara, H.A., Barwey, S., Galassi, R.M., Malik, M.R., Val-orani, M., Raman, V., Im, H.G.: A data-driven reduced-order model for stiff chemical kinetics using dynamics-informed training. *Energy and AI* **15**, 100325 (2024)
- [38] Cybenko, G.: Approximation by superpositions of a sigmoidal function. *Mathematics of control, signals and systems* **2**(4), 303–314 (1989)

- [39] Mhaskar, H.N.: Neural networks for optimal approximation of smooth and analytic functions. *Neural computation* **8**(1), 164–177 (1996)
- [40] Siegel, J.W., Xu, J.: Approximation rates for neural networks with general activation functions. *Neural Networks* **128**, 313–321 (2020)
- [41] Ha, D., Dai, A.M., Le, Q.V.: Hypernetworks. In: International Conference on Learning Representations (2017). <https://openreview.net/forum?id=rkpACe1lx>
- [42] Hernandez, Q., Badias, A., Gonzalez, D., Chinesta, F., Cueto, E.: Structure-preserving neural networks. *Journal of Computational Physics* **426**, 109950 (2021)
- [43] Lee, K., Trask, N., Stinis, P.: Machine learning structure preserving brackets for forecasting irreversible processes. *Advances in Neural Information Processing Systems* **34**, 5696–5707 (2021)
- [44] Lee, J.Y., Cho, S., Hwang, H.J.: Hyperdeeponet: learning operator with complex target function space using the limited resources via hypernetwork. In: The Eleventh International Conference on Learning Representations (2022)
- [45] Conti, P., Gobat, G., Fresca, S., Manzoni, A., Frangi, A.: Reduced order modeling of parametrized systems through autoencoders and sindy approach: continuation of periodic solutions. *Computer Methods in Applied Mechanics and Engineering* **411**, 116072 (2023)
- [46] Paszke, A., Gross, S., Massa, F., Lerer, A., Bradbury, J., Chanan, G., Killeen, T., Lin, Z., Gimelshein, N., Antiga, L., et al.: PyTorch: An imperative style, high-performance deep learning library. *Advances in neural information processing systems* **32** (2019)
- [47] Bradbury, J., Frostig, R., Hawkins, P., Johnson, M.J., Leary, C., Maclaurin, D., Necula, G., Paszke, A., VanderPlas, J., Wanderman-Milne, S., et al.: JAX: composable transformations of python+ numpy programs (2018)
- [48] Kingma, D.P., Ba, J.: Adam: A method for stochastic optimization. preprint arXiv:1412.6980 (2014)
- [49] Schroeder, D.V.: An introduction to thermal physics. American Association of Physics Teachers (1999)
- [50] Shang, X., Öttinger, H.C.: Structure-preserving integrators for dissipative systems based on reversible–irreversible splitting. *Proceedings of the Royal Society A* **476**(2234), 20190446 (2020)
- [51] Ng, A., *et al.*: Sparse autoencoder. *CS294A Lecture notes* **72**(2011), 1–19 (2011)
- [52] Bris, C.L., Lelievre, T.: Multiscale modelling of complex fluids: a mathematical

initiation. *Multiscale modeling and simulation in science*, 49–137 (2009)

- [53] Virtanen, P., Gommers, R., Oliphant, T.E., Haberland, M., Reddy, T., Cournapeau, D., Burovski, E., Peterson, P., Weckesser, W., Bright, J., *et al.*: SciPy 1.0: fundamental algorithms for scientific computing in python. *Nature methods* **17**(3), 261–272 (2020)